



OPEN

Aqueous phase adsorption of phenothiazine derivative onto zinc oxide doped activated carbon

Clement O. Obadim¹, Solomon E. Shaibu², Godwin N. Enin², Ekemini B. Ituen³, Idongesit B. Anweting², Uwem U. Ubong¹, Ifiok O. Ekwere¹, Saeed G. Adewusi⁴, Tijesu J. Adeoye⁵, Dele P. Fapajuwo⁶, Utibe A. Ofon⁷, Opeyemi K. Fatunla⁷, Nathaniel S. Essien², Oluwatosin. Y. Audu⁸, Zenixole R. Tshentu⁶, Simphiwe M. Nelana⁹, Michael J. Klink⁹ & Olushola S. Ayanda¹⁰✉

Plant-mediated synthesis of nanoparticles is a sustainable approach that has gained widespread scientific acceptance due to its numerous benefits and applications. In this study, a zinc oxide-doped activated carbon (ZAC) derived from palm kernel shells (PKS) was synthesized via a bioreduction route using a water-based extract of *Nymphaea lotus* leaves as a reducing agent. The synthesized ZAC nanocomposites were characterized using microscopic (TEM, SEM) and spectroscopic (FTIR, EDS, XRD, and UV-Vis) analyses. The adsorptive properties of ZAC and efficiency in scavenging a phenothiazine derivative (methylene blue) from an aqueous solution were investigated. Results reveal that nano-scale ZAC particles were crystalline, exhibited irregular shapes, with an average size of 45 nm, and were highly dispersed. The optimum quantity adsorbed was 248 mg/g at a methylene blue concentration of 140 mg/L for 60 min using 0.02 g/100 mL of ZAC. Adsorption and kinetics data closely aligned with the Freundlich isotherm and the pseudo-second-order model, respectively indicating heterogeneous surface adsorption and chemisorption as the dominant mechanisms. The regeneration study of ZAC shows that over five cycles, thermal regeneration maintained high adsorption capacity with minimal decline and chemical regeneration significantly led to reduction in the adsorption capacity but solvent washing offered a balance between efficacy and structural preservation.

Keywords Methylene blue dye, Nanocomposite, Adsorption, Zinc-doped palm kernel, *Nymphaea lotus*

The textile industry has experienced significant growth, along with its associated industries, which has had a positive impact on the economies of many countries. However, this growth has also resulted in significant environmental consequences^{1,2}. One of the key environmental concerns is the pollution of water, which serves as a major receptor and transporter of industrial effluents. It is crucial to ensure the preservation of water quality. The boom in the textile industries has positively stimulated the economy of many countries but not without leaving glaring environmental footprints. Prominent among the environmental matrix that receives and transports the bulk of industrial effluent is water and it is often needed in good state². The textile industry is reported to be one of the industries known to consume huge quantities of water^{3,4}. In this industry, dyes are the major materials used, there are between 100,000 to 150,000 commercially available dyes and about 800,000 tons are manufactured annually⁵. Within this quantity, more than 10% is indiscriminately discharged into water

¹Department of Chemistry, Akwa Ibom State University, Ikot Akpaden, Nigeria. ²Department of Chemistry, University of Uyo, Uyo, Nigeria. ³Emerging Materials and Energy Group, Department of Chemistry, University of Uyo, Uyo, Nigeria. ⁴Department of Chemistry, School of Sciences, Federal University of Education, Zaria, Nigeria. ⁵Department of Chemistry, University of Vermont, Burlington, VT 05405, USA. ⁶Department of Chemistry, Nelson Mandela University, Port Elizabeth, South Africa. ⁷Department of Microbiology, University of Uyo, Uyo, Nigeria. ⁸Drug Discovery and Development Centre (H3D), Department of Chemistry, University of Cape Town, Rondebosch 7701, Cape Town, South Africa. ⁹Department of Chemistry, Vaal University of Technology, Vanderbijlpark, South Africa. ¹⁰Department of Chemistry, Federal University Oye-Ekiti, Oye-Ekiti, Nigeria. ✉email: osayanda@gmail.com

bodies⁶. The deleterious effects of dyes that are present in textile effluent are well-documented including but not limited to nausea, obstruction of photosynthesis⁵, headache⁶, carcinogenicity⁴, and mutagenicity⁷. Methylene blue (MB), which is the first phenothiazine derivative to be synthesized and a key dyestuff in the textile industry, is particularly responsible for a wide range of health-related challenges ranging from mental fatigue, lethargy, skin inflammation common respiratory issues to teratogenic effects^{8,9}. It is a widely used model cationic dye for agricultural, cosmetics, laboratory, and pharmaceutical applications. Due to its complex structural and functional frame, MB has been reported to be non-biodegradable, highly mobile, and recalcitrant¹⁰.

Over the years, numerous remediation techniques for the removal of aqueous contaminants have been reported and some of these include coagulation, electrocoagulation, adsorption, precipitation, ion exchange, reverse osmosis, filtration, photocatalysis, and other biological treatment retraining with reasonable success^{11–14}. By extension, Nassar et al. 2023, used a facile hydrothermally synthesised photocatalyst (nanocomposite) to photocatalytically degrade MB dye by about 92.5% in 55 min¹⁵ which is quite similar to the 98.5% degradation efficiency recorded by Aljohani et al. 2021 in 90 min when they used cobalt aluminate/carbon composite nanoparticles prepared via auto-combustion route to remove MB dye from aqueous media¹⁶. These studies vividly depict the efficiency of removal of MB using photocatalytic approach, but not without its attendant drawbacks^{15,16}. In a different study, Meselhy et al. 2024, employed auto-combustion method to synthesise lanthanum-doped TiO₂ nanostructures but for the photoctalytic degradation of a different dye (crystal violet dye) and still reported a high efficiency of 95.98% in 70 min while also varying dopant percentages¹⁷. However, the attendant drawbacks connected with some of these treatment options include the generation of secondary pollution, environmental degradation, and expensive nature, others include the complexity of technique and maintenance related issues³. Comparatively, adsorption is well embraced in the scientific community as well as industry due to its simplicity, cost-effectiveness, and efficiency¹⁸ which substantiates its widespread deployment in several studies involving the removal of toxic materials from various aqueous media and the present study. This was depicted in the study by Nassar et al. 2016 who investigated the effect of counterions on hydrothermally synthesized hydrozincite (zinc hydroxide carbonate). It was reported that the hydrozincite was subsequently converted to generate ZnO nanostructures via thermal means, and applied for the removal of Reactive Black 5 (RB5) dye from wastewater which achieved about 81 mgg⁻¹ adsorption capacity¹⁹.

Nanotechnology is an emerging revolution in the water treatment industry; the adoption of an environmentally benign approach to produce nanomaterials is on the front burner globally². The benign synthesis of nanocomposites using plant extracts is highly advocated in view of ease of operation, cheapness, rapid and eco-friendly nature including tunability^{10,20}. Many plant extracts have been successfully used to synthesize nanocomposites²¹. As far as the plant used does not compete with food, it may be considered suitable for the synthesis. Recently, Nassar et al. 2014, synthesised silver nanoparticles using lemon leaf extract as both reducing and stabilising agent and the process was fast, cost-effective and environmentally friendly²². Also, different agricultural biomass like *Vateria indica* fruits²³, pods of copper pod tree²⁴ and *Cynometra ramiflora* fruits²⁵ have been used to prepare biochars ((BC-Fe₃O₄, CPAC@Fe₃O₄ and activated carbon) and systematically applied for the removal of MB, 2,4-dichloro phenylacetic acid (2,4-D) and tetracycline, respectively with impressive results.

The plant used for the present study, *Nymphaea lotus*, is a flowering plant from the family *Nymphaeaceae*. The *Nymphaea lotus* is a predominant plant in East Africa and Southeast Asia and as such cannot be explored holistically in other regions of the world. It is very accessible and abundant in various parts of Nigeria and Africa, and its composition as posited by researchers contains many biomolecules from saponins to phenols^{26,27}. Similarly, the capping and functionalization properties of these organic moieties impart the functionalities of the nanocomposites while the palm kernel shells (PKS) ash provides support for the zinc nanoparticles to reduce rapid agglomeration during and after synthesis. The novelty of the current study lies in the use of *Nymphaea lotus* extract as a reducing agent as well as the doping of PKS activated carbon onto zinc oxide via a biological route. This study addresses the gap in sustainable water treatment technique by synthesizing zinc oxide-doped activated carbon (ZAC) using PKS, metal precursor and *Nymphaea lotus* leaf extract. The novelty lies in the twofold approach of using *Nymphaea lotus* extract as a reducing agent and doping PKS activated carbon with zinc oxide via a green route.

In this study, ZAC was synthesized using PKS and *Nymphaea lotus* aqueous leaf extract acting as reducing agent followed by application for the sequestration of MB from different aqueous media. At the same time, the adsorption kinetics, thermodynamic and reusability potentials of the ZAC nanocomposites were elucidated.

Material and methods

Chemicals and reagents

The *Nymphaea lotus* was identified by a taxonomist prior to the extraction and preliminary assessment as previously documented^{28,29}. The collection and use of the plant conform to relevant guidelines and regulations. Analytical (Analar) grade chemicals were used throughout this study, some of which include Zn(OH)₂ (Merck analysis grade), MB (BDH prd No. 340484B), NaOH and HCl (Sigma Aldrich). All stock solutions were prepared with deionized water and other concentrations via serial dilution. The residual MB after adsorption study was evaluated at λ_{max} of 665 nm using a Beckman Coulter, Pasadena, CA, UV-Vis spectrophotometer (DU 730).

Materials preparation

The PKS sourced from the Uyo metropolis market in Akwa Ibom State, Nigeria, were washed thoroughly with deionized water, dried for 24 h at 28 ± 2 °C, cut, and then ground into a fine powder. Following a 4-h soak in 0.1 M HCl solution, it was thoroughly cleaned with deionized water, then dried at 28 ± 2 °C, and subjected to carbonation and chemical activation as described by Adebayo and his co-workers³⁰. The PKS were heated in a muffle furnace for about 4 h at 400 °C, then cooled to room temperature to begin the precarbonization process.

In order to create a homogeneous mix, it was weighed at 50 g and stirred with 250 mL of an aqueous solution of 85% H_3PO_4 for 4 h. The slurry was first dried for 24 h at 110 °C, then heated for 2 h at 800 °C, and cooled. To obtain the finished product, it was dried at 110 °C after being washed many times with hot water to neutrality and finally with cold water to eliminate any remaining phosphoric acid.

The *Nymphaea lotus* leaves were collected, washed in deionized water, dried at 28 ± 2 °C for 48 h, and then macerated. In line with previous reported methods^{29,31}, 30 g of the macerated *Nymphaea lotus* leaves were boiled for 10 min, filtered and the resultant broth was kept at 4 °C before use for synthesis.

The ZAC was prepared by adding 5 g of PKS activated carbon to a 100 mL solution of 3.0 M $Zn(OH)_2$ (29.82 g in 100 mL of deionized water), stirred continually for 30 min, and 100 mL of the *Nymphaea lotus* plant extract was added at its natural pH. The mixture was agitated for an additional 120 min at 350 rpm and in order to complete the bioreduction process, it was left to stand for 48 h after which a colour change from off-white to pale yellow was observed followed by filtration. The resulting ZAC was dried in an oven at 45 °C and ground before characterization³².

Characterization of zinc oxide-doped activated carbon nanocomposite

The samples were analyzed by transmission electron microscopy (TEM) and scanning electron microscopy (SEM) to examine their surface characteristics, sizes, and shapes. The functional groups were identified using FTIR H400I Shimadzu. UV-Vis scan was employed to monitor the level of residual MB prior to and after the adsorption process. X-ray diffraction (XRD) analysis was conducted using a Rich Sievert 3000 diffractometer to assess the phase purity of activated carbon (AC) and ZAC within a specific range that covered the major species of zinc and AC. The Scherrer equation, as presented in Eq. (1), was utilized to provide more clarification of the diffractogram.

$$CS = K\lambda/\beta \cos \theta \quad (1)$$

where CS is the crystallite size, $[\beta] = FWHM \times \pi/180$, $\lambda = 1.5406 \times 10^{-10}$, Constant $[K] = 0.94$, and $\cos \theta$ = Bragg angle (Raliya et al. 2014).

Adsorption experiments and isotherms

The experiment focused on the removal of MB from water using ZAC at approximately 27 ± 2 °C. Different amounts of ZAC were mixed with varying concentrations of the aqueous solution, agitated, and subsequently centrifuged to determine the remaining MB concentration. The quantity of MB adsorbed was calculated using Eq. (2). To ensure accuracy, the measurements were done in triplicates with the average results reported.

$$Q_e = \frac{(C_0 - C_e)}{w} \times V \quad (2)$$

The starting and equilibrium concentrations (mg/L) are C_0 and C_e , respectively. V denotes the volume of the MB solution (L), whereas w signifies the mass of the ZAC (g).

The often-employed models for describing two-parameter systems for adsorption are those of Langmuir, Freundlich, and Temkin³³. The Langmuir isotherm, as represented by Eq. (3), postulates the occurrence of monolayer adsorption on a uniform surface. In contrast, the Freundlich isotherm (Eq. 4) describes a heterogeneous system with an uneven surface, allowing for the formation of multiple layers of adsorbate on the adsorbent. However, the Freundlich isotherm is applicable only at low concentrations of the adsorbate, as noted by Majd et al.³³. The Temkin model (Eq. 5) considers the interaction between the adsorbent and adsorbate, making it particularly suitable for forecasting gas phase equilibrium, but may not be adequate for other types of systems^{10,33}. In this work, models of Temkin, Langmuir, and Freundlich isotherms were employed to examine the adsorption data using their respective equations.

$$\frac{C_e}{Q_e} = \frac{1}{Q_0 K_L} + \frac{1}{Q_0} C_e \quad (3)$$

$$R_L = \frac{1}{1 + K_L C_0} \quad (3a)$$

$$\log Q_e = \log K_f + \frac{1}{n} \log C_e \quad (4)$$

$$Q_e = \frac{RT}{b_r} \ln A_r + \frac{RT}{b_r} \ln C_e \quad (5)$$

In the above equations, the equilibrium concentration (C_e) of MB is measured in mg/L, C_0 represents the starting concentration (mg/L) of MB, Q_e represents the amount of adsorbate per unit mass adsorbed (mg/g), and Q_0 represents the adsorption capacity (mg/g). Also, the Langmuir equilibrium adsorption constant (K_L) included in Eq. (3a) is dimensionless and serves as an indicator of the level of favorability exhibited by the Langmuir isotherm curve. Specifically, the R_L parameter is classified as unfavourable when its value exceeds 1, linear when it equals 1, favourable when it falls within the range of 0–1, and irreversible when it equals zero³². The constants in the Freundlich model, K_f and n , also act as measures of whether the adsorption is favorable or otherwise. Here, K_f indicates the capacity of the adsorbent to adsorb. Insights into the adsorption mechanism can be obtained

by deducing information from the Eq. (5), where equilibrium binding constant is A_p , the isotherm constant b_T , the universal gas constant R (8.314 J/mol/K), and the absolute temperature T (298 K). Other models were also utilized to investigate the adsorption kinetics, and they include pseudo-first order (Eq. 6), pseudo-second order (Eq. 7), and the Elovich (Eq. 8) models.

$$\log(Q_e - Q_t) = \log Q_{e,cal} - \frac{k_1}{2.303} t \quad (6)$$

$$\frac{t}{Q_t} = \frac{1}{k_2 Q_{e,cal}^2} + \frac{1}{Q_{e,cal}} t \quad (7)$$

$$Qt = \frac{1}{\beta} \ln \frac{\alpha_E}{\beta} + \frac{1}{\beta} \ln t \quad (8)$$

In Eqs. (6)–(8), the quantities of adsorbates that have been adsorbed (measured in mg/g) at equilibrium and at a certain time t are Q_e and Q_t , respectively. On the other hand, k_1 , k_2 , α , and β denote the constants associated with the Eqs. (6)–(8) accordingly.

Results and discussion

Size, shape, and dispersion features of zinc oxide-doped activated carbon nanocomposite

The images of ZAC as determined by TEM are displayed in Fig. 1. These images reveal a vast dispersion of predominantly irregular zinc nanoparticles that are primarily less than 100 nm in size, supported by AC. The form, size, and distribution pattern of the ZnO nanoparticles on the AC (Fig. 1a) are greatly dependent on the nature of *Nymphaea lotus* extract and experimental settings. The obtained nanoparticles were well dispersed with no observable particle pairing inclinations or groupings. This could be attributed to the coating capacities of the phytochemicals of *Nymphaea lotus* leaf extract, which expand their surface area according to Phanjom and associates³⁴. In a departure from the views of Phanjom and associates, flavonoids and, more specifically, phenols were proven to deter clustering owing to their unique reduction and enveloping abilities, a claim that also gained support from other authors^{35,36}.

SEM was used to investigate the morphologies of AC and ZAC and the obtained micrographs are presented in Fig. 2a,b. A greater number of notches and a stacking phenomenon were observed in ZAC particles (Fig. 2b), mostly attributed to the bioactive components from the *Nymphaea lotus* leaf extract. This theory aligns with the opinion of Shaibu and coworkers²⁰. When compared to ZAC (Fig. 2b), a notable clustering was evident with the AC sample. Conversely, ZAC showed signs of singular particles, exhibiting a lower extent of agglomeration due to the shielding action of the biomolecules in the *Nymphaea lotus* as recently proposed³⁷. An irregular particle shape and an average size ranging from 45 to 60 nm were depicted in the ZAC micrograph in Fig. 2b.

Elemental composition of zinc oxide-doped activated carbon nanocomposite

The EDX spectra (Fig. 3) reveal the presence of zinc alongside other elements (Si, Al, K, O, and Fe) in the precursors utilized for ZAC formulation. Consistent findings across Fig. 3a,b depict the elemental makeup of the AC and ZAC to notably include high percentages of C, O, N, S, and Zn. The oxygen and zinc composition were greater in ZAC compared to AC, and the source of this may be attributed to oxygen-containing organic groups present in the *Nymphaea lotus* extract. This observation agrees with the findings reported by Roseline and co-workers³⁶. Figure 3b also reveals an inset of the layered image of ZAC depicting the elemental electron

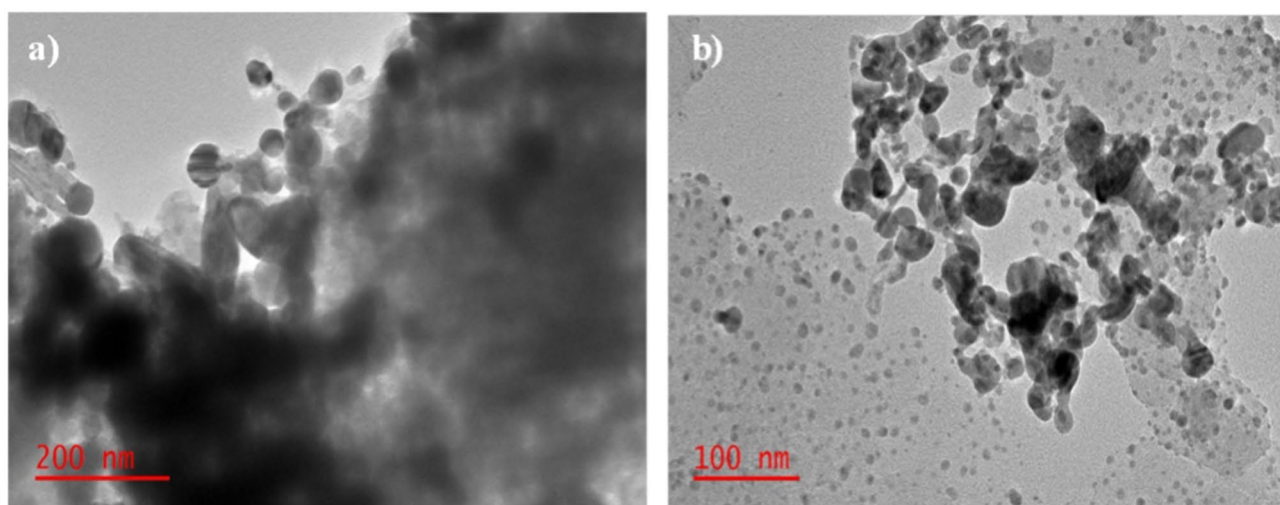


Fig. 1. TEM images showing the size, shape, and dispersion of zinc oxide-doped activated carbon nanocomposite at (a) 200 nm and (b) 100 nm.

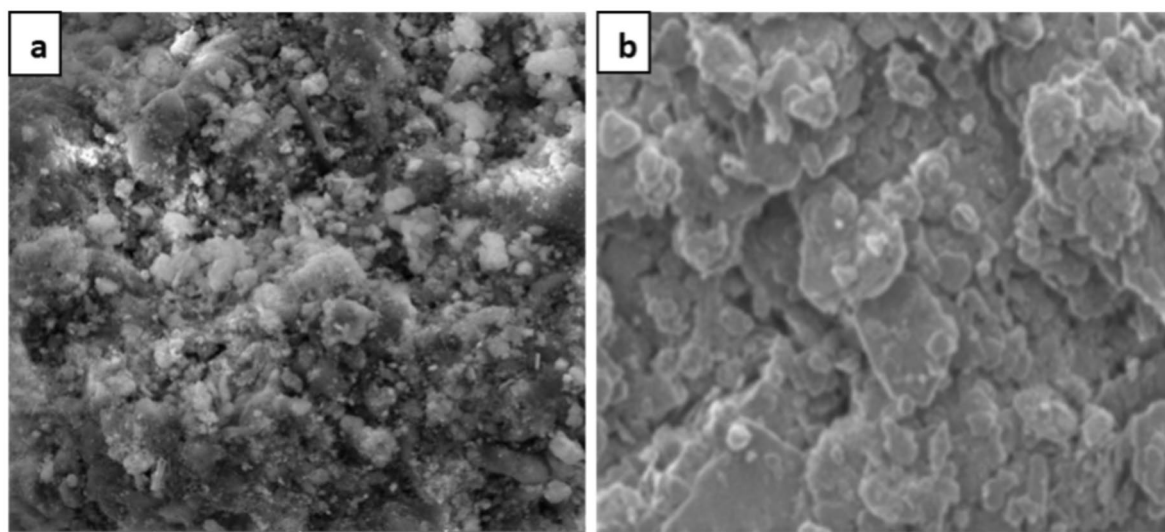


Fig. 2. Morphological features of (a) activated carbon and (b) zinc oxide-doped activated carbon nanocomposite.

representation of selected elements. Moreover, the individual mapping of the selected elements in ZAC is shown in Fig. 3c,h.

Crystallographic analysis of zinc oxide-doped activated carbon nanocomposite

The XRD pattern displays distinct diffraction peaks that can be attributed to the hexagonal close-packed (HCP) structure of zinc oxide nanoparticles, as illustrated in Fig. 4. The peak at 26.45° (002) in the XRD pattern of ZAC indicates the presence of activated carbon. This peak can be attributed to the amorphous carbon structures present in the sample. The observed diffraction peaks at angles of 36.01° , 39.11° , 46.41° , 55.9° , and 70.1° correspond to diffraction from the (002), (100), (101), (102), and (103) crystallographic planes of a hexagonal close-packed (HCP) structure, respectively. The alignment of the hexagonal closed pack structure of zinc oxide nanoparticles with the JCPDS number 00-004-0784 is observed. The size of zinc oxide (ZnO) nanoparticles was determined using Debye Sherrer's formula (Eq. 1). The resulting average size of ZnO nanoparticles was approximately 45 nm. This in agreement with other authors' submission^{35,36}.

Elucidation of functional groups in zinc oxide-doped activated carbon nanocomposite

The functional groups in ZAC are significantly enhanced by the interactions between *Nymphaea lotus* extract and the active sites present on its surface^{37–39}, as illustrated in the FTIR spectrum shown in Fig. 5. The absorption bands observed at wave numbers of 3604 cm^{-1} , 3401 cm^{-1} , 2823 cm^{-1} and 1620 cm^{-1} can be assigned to the $-\text{Al}-\text{OH}$, $\text{O}-\text{H}$ amide group, $-\text{CH}_2$ bending vibration, and $-\text{C}=\text{O}$ groups, correspondingly. Additionally, the $\text{Zn}-\text{O}$ bands within the range of 1150 cm^{-1} – 950 cm^{-1} observed in the spectrum are associated with the AC properties. The absorption bands seen at around 3650 and 1620 cm^{-1} may be correlated with the stretching and bending vibrations of $\text{Zn}-\text{Zn}-\text{OH}$ bonds and water molecules, respectively. These observations are mostly ascribed to the utilization of *Nymphaea lotus* extract and the wet synthesis process, as previously suggested¹⁶. Biomolecules present in the *Nymphaea lotus* leaf extract, as well as the AC and zinc nanoparticle, resulted in a significant and downward shift of the ZAC spectrum, indicating a strong interaction between these components. Roseline and co-workers proposed that the existence of negatively charged functional groups on the periphery of ZAC may potentially augment the adsorption ability for cations³⁶ which supports the removal efficiency of ZAC in the adsorption study.

UV-Vis analysis

For many years, UV-Vis spectroscopy has been recognized for its ease in detecting changes due to shifts in energy levels when suitable wavelength radiation is absorbed⁹. When *Nymphaea lotus* extract was introduced, the formation of ZAC was clearly observable through a change to a slightly yellow color, which aligns with the previous findings³⁸. In the ZAC spectrum (Fig. 6), an additional distinct absorption peak around 350 nm , which is missing in the spectrum of AC that has a prominent band at 240 nm , corresponds to the surface plasmon resonance band of ZnO nanoparticles as corroborated by Fakhari and co-workers⁴⁰.

Adsorption studies

The effects of different experimental factors on the adsorption efficiency were probed via adsorption studies. These factors include but are not limited to initial MB concentration, ZAC dosage, solution pH, and contact time.

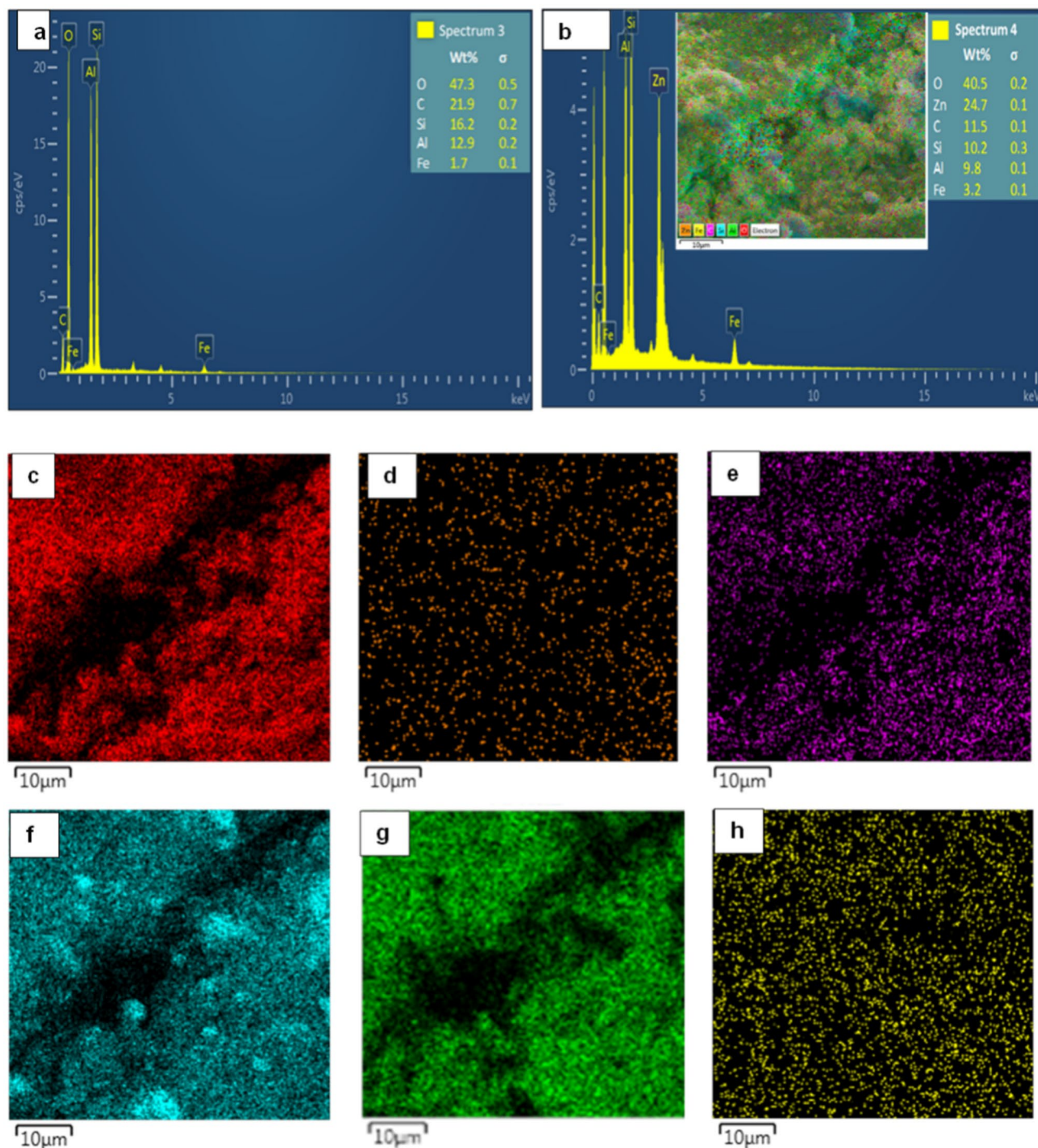


Fig. 3. Elemental composition of (a) activated carbon (b) zinc oxide-doped activated carbon nanocomposite with EDS layered inset; electron mapping of (c) O (d) Zn (e) C (f) Si (g) Al and (h) Fe atoms on the surface.

Initial concentration

The initial concentration of adsorbate is a critical factor influencing adsorption, particularly for optimization in environmental remediation processes. This principle is clearly demonstrated in the relationship between the quantity of MB removed from the reaction medium and its initial concentration. This direct relationship is indicative of ZAC's proficiency in overcoming mass transfer resistance, emphasizing findings similar to those reported³⁸. At a lower initial concentration of 10 mg/L MB, the limited number of MB molecules, when compared with the abundance of pores, functional groups, and adsorption sites on ZAC, results in an inefficient adsorption process. This phenomenon can be explained from the angle of adsorption kinetics, where the rate of MB uptake is initially slow due to limited collisions between adsorbate and adsorbent. However, as the MB concentration increases from 30 to 140 mg/L, the dynamics of adsorption shift significantly. The escalating concentration creates

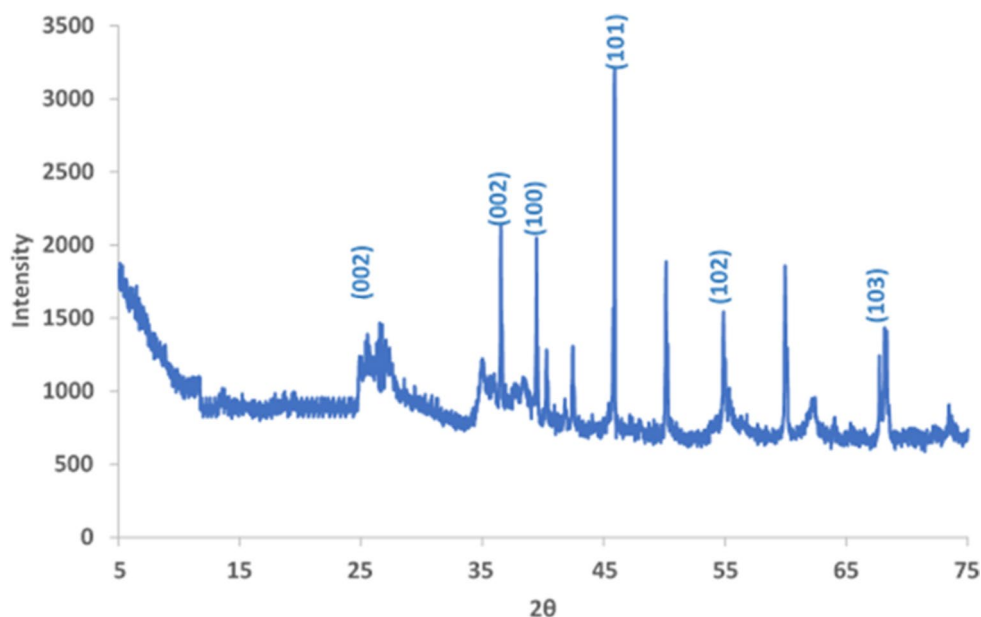


Fig. 4. XRD diffraction pattern of zinc oxide-doped activated carbon nanocomposite.

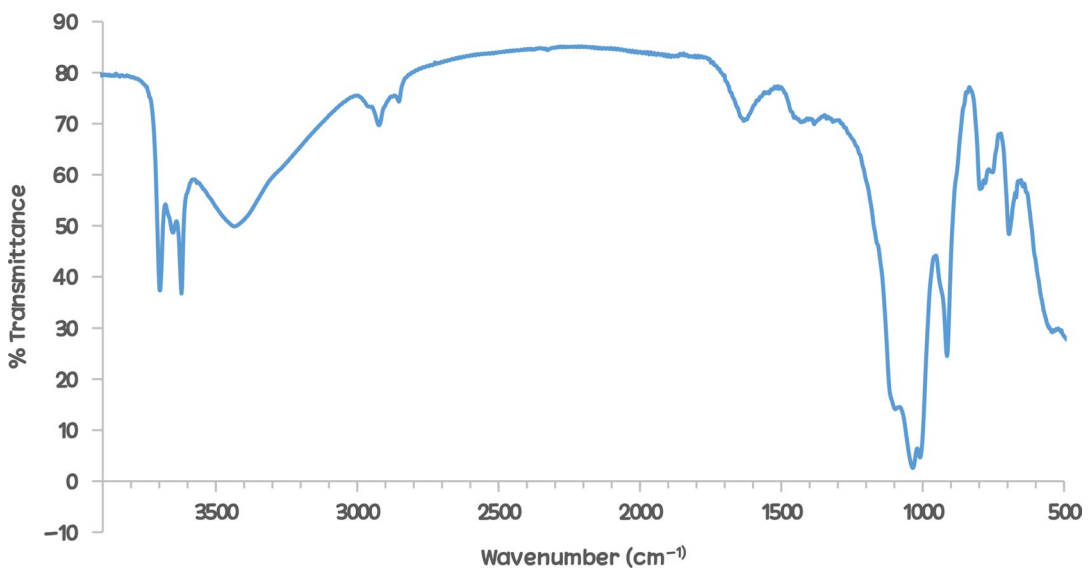


Fig. 5. FTIR spectrum of zinc oxide-doped activated carbon nanocomposite.

a driving force strong enough to surpass the initial mass transfer resistance. This phenomenon is reflected in the noticeable increase in MB removal, peaking at an adsorption capacity of 254 mg/g (Fig. 7a). The increase in adsorption with concentration can be attributed to the enhanced probability of collision and subsequent adsorption between the MB molecules and ZAC. This linear increase aligns with Langmuir isotherm models, indicating a monolayer adsorption process on a homogenous surface with finite adsorption sites. Singh et al.⁴¹ further elucidate this by linking the linear adsorption trend to changes in the interfacial distribution coefficient, which accounts for the equilibrium concentration of MB on ZAC compared to the solution. As the concentration of MB in the solution increases, the distribution coefficient adjusts to maintain equilibrium, leading to higher adsorption until saturation is reached. The plateau at 140 mg/L is indicative of a saturation point where the active sites on ZAC are fully occupied, aligning with the Langmuir isotherm's prediction of a monolayer saturation point. This saturation leads to molecular transport interference, as the available sites on ZAC are fully occupied, preventing further adsorption and resulting in a stable adsorption capacity despite increases in MB concentration beyond this point.

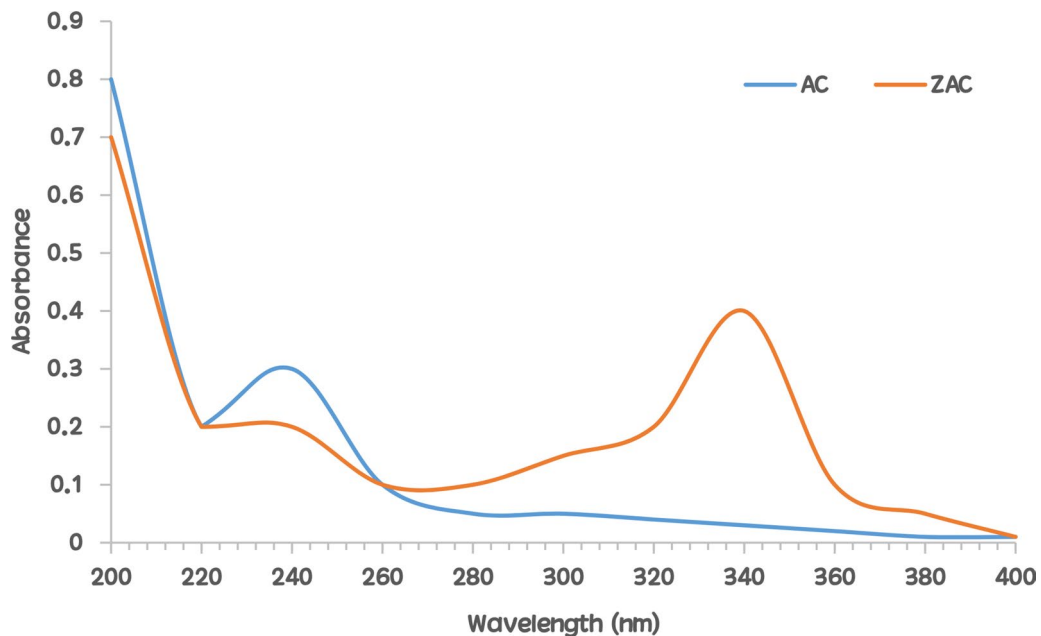


Fig. 6. UV-Vis spectra showing the surface plasmon resonance band of activated carbon and zinc oxide-doped activated carbon nanocomposite.

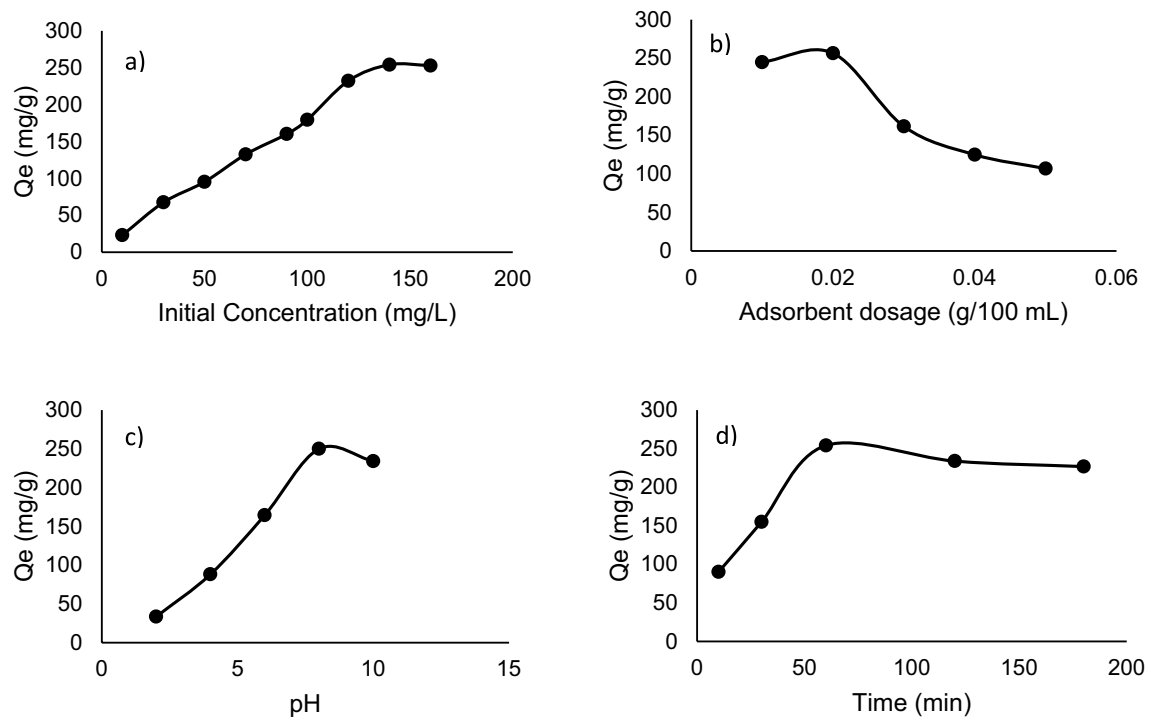


Fig. 7. (a) Effect of conc ($w=0.02$ g/100 mL/100 mL, pH 5, temp = 27 ± 2 °C for 2 h at 200 rpm), (b) Effect of adsorbent dosage ($C_0=140$ mg/l, pH 5, temp = 27 ± 2 °C for 2 h at 200 rpm), (c) Effect of time ($C_0=140$ mg/l, $w=0.02$ g/100 mL, temp = 27 ± 2 °C for 2 h at 200 rpm) and (d) Effect of time ($w=0.02$ g/100 mL, pH 4, $C_0=140$ mg/l, temp = 27 ± 2 °C at 200 rpm).

Adsorbent dosage

The process of identifying the optimal dosage of ZAC for the effective adsorption of a target MB concentration involves a careful balance between maximizing adsorption efficiency and economic viability. As depicted in Fig. 7b, the adsorption capacity increases with the ZAC dosage up to 0.02 g/100 mL, beyond which no significant enhancement in MB removal was observed. This trend can be attributed to the increased surface area and

availability of more active adsorption sites at optimal ZAC dosages. However, at concentrations between 0.01 and 0.02 g/100 mL, the adsorption process may encounter limitations due to steric hindrance and electrostatic interactions within the MB complex. These interactions can obstruct the binding of additional MB molecules to available adsorption sites, leading to a saturation point. Additionally, the kinetics of the adsorption process are influenced by the size and morphology of ZAC particles. Smaller particles tend to have a higher surface area-to-volume ratio, providing more active sites for adsorption. However, as noted by Awe et al.⁴², at higher adsorbent concentrations, the likelihood of particle aggregation increases, reducing the effective surface area of ZAC and elongating the diffusion pathways. This phenomenon adversely affects the adsorption efficiency as it increases the resistance to mass transfer and slows down the adsorption kinetics. The interaction between ZAC and MB is not only a function of surface interactions but also of the changes in the energy and disorder of the system⁴³. A comprehensive understanding of these parameters is essential for optimizing the adsorption process and ensuring efficient MB removal from aqueous solutions. Therefore, achieving the optimal dosage of ZAC for MB adsorption is a complex interplay of adsorbent concentration, particle characteristics, and the thermodynamic and kinetic properties of the adsorption system. This interplay dictates the efficiency and effectiveness of the adsorption process, as seen in the plateauing effect beyond ZAC concentration of 0.02 g/100 mL.

pH

The adsorption capacity of ZAC is significantly influenced by the solution's pH, which acts as a critical factor in dictating the chemistry at the adsorbent-adsorbate interface^{43,44}. In this study, the impact of pH on the adsorption of MB was thoroughly investigated. The experiment involved adjusting the pH of an MB solution (concentration 140 mg/L) between 2 and 10 and observing the adsorption behavior over 60 min periods with 0.02 g/100 mL of ZAC. The results, illustrated in Fig. 7c, showed a clear correlation between the pH level and the adsorption efficiency. At lower pH levels, particularly around 2, there was a notable reduction in the quantity of MB adsorbed by ZAC. This decrease can be attributed to the high concentration of H⁺ ions in the solution, which likely competed with the positive MB ions (MB⁺) for adsorption sites on ZAC. The presence of these excess H⁺ ions in an acidic environment may lead to a decrease in the availability of functional groups on ZAC for binding with MB, resulting in lower adsorption rates.

As the pH increased, particularly beyond pH 7, a significant increase in the adsorption of MB was observed, peaking around pH 8. This enhancement at higher pH levels can be explained by the increased negative charge on the surface groups of ZAC. In alkaline conditions, these groups become more polarized, enhancing electrostatic interactions between the positively charged MB ions and the negatively charged sites on ZAC. This leads to more effective sequestration of MB from the solution, as the complementary charges facilitate stronger adsorbent-adsorbate interactions. These findings are in line with the notion that the surface charge of the adsorbent, and consequently its adsorption capacity, is heavily influenced by the pH of the solution^{43,44}. This pH-dependent behavior underscores the importance of optimizing solution pH for maximizing adsorption efficiency in practical applications.

Contact time

In order to elucidate the kinetics of MB uptake by ZAC, the contact time between the adsorbent and adsorbate was systematically varied. Initially, there was a rapid increase in the quantity of MB removed, escalating from 90 mg/g at 20 min to a peak of 254 mg/g at 60 min. After this peak, the adsorption rate decelerated, reaching a plateau and equilibrium at 226 mg/g, as illustrated in Fig. 7d. This trend is primarily attributed to the expansive surface area of ZAC and the availability of numerous unoccupied sites at the beginning of the adsorption process. However, these sites quickly became saturated after approximately 60 min of contact with MB. The rapid saturation of ZAC could be linked to steric hindrance and the inertia of diffusion exhibited by MB molecules as the contact time prolongs. This aligns with the pseudo-second-order kinetic model, suggesting that the adsorption rate is more dependent on the availability of adsorption sites than the concentration of MB. Furthermore, the declining rate of adsorption beyond 60 min may be indicative of intraparticle diffusion constraints, a phenomenon that aligns with trends observed in similar studies¹⁴. Additionally, the involvement of both physisorption and chemisorption processes in the adsorption mechanism, as supported by empirical evidence in literature⁴⁵, provides a comprehensive understanding of the dynamic interaction between ZAC and MB over varied time scales.

Adsorption isotherms

An adsorption isotherm depicts the equilibrium correlation between the concentration of the solute in a liquid phase and quantity of solute adsorbed on a solid phase under constant temperature conditions³³. The suitability of any adsorption model is usually dependent on the magnitude of coefficient of correlation (R^2) obtained from the linear plots (Fig. 8). Results obtained from the adsorption isotherms (Table 1) for the adsorption of MB on the ZAC reveals that of the three models, the Freundlich model passed as the best with R^2 of 0.9931 as the closest to unity. The value of the Freundlich parameter, n , was greater than 1, indicative of a favourable adsorption⁶. This was further corroborated by the separation factor's (R_L) numerical value in the Langmuir's model. This value was 0.3539 (i.e. $0 < R_L < 1$) corresponding to favourable adsorption. The adsorption of MB was also found to be feasible based on the model^{14,30}. The adsorption energy from Temkin's model was positive for MB in aqueous media indicating endothermicity of the adsorption process⁷.

Kinetic study

Kinetic models are often used for predicting the rate and time dependency of reactions in various scientific and engineering domains, particularly in understanding the mechanistic behaviors of chemical and biological

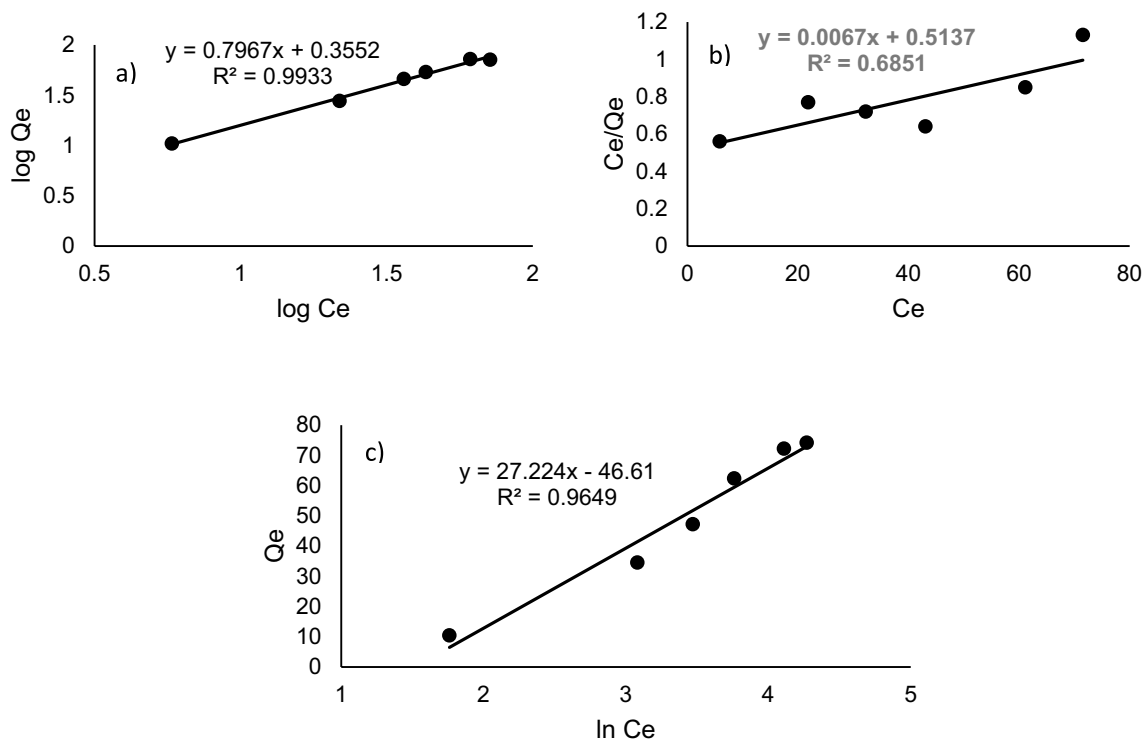


Fig. 8. Isotherm models of (a) Freundlich (b) Langmuir and (c) Temkin.

Adsorption isotherms	Parameters	Values
Freundlich model	K_f (mg/g(L/mg) ^{1/n})	1.7041
	n	1.1357
	R^2	0.9931
Langmuir model	Q_0 (mg/g)	149.2537
	K_L	0.0130
	R_L	0.3539
	R^2	0.6851
Temkin model	A_T (L/g)	0.1805
	b_T	83.3721
	R^2	0.9649

Table 1. Adsorption parameters deduced from the adsorption isotherms for the sequestration of MB by zinc oxide-doped activated carbon nanocomposite.

Kinetic models	Parameters	Values
Pseudo-first-order	k_1 (min ⁻¹)	0.0313
	$Q_{e,cal}$ (mg/g)	40.1051
	R^2	0.9658
Pseudo-second-order	k_2 (g/mg/min)	0.0016
	$Q_{e,cal}$ (mg/g)	237.719
	R^2	0.9991
Elovich	β (g min/mg)	0.1169
	α_E (g min ² /mg)	14.2958
	R^2	0.9793

Table 2. Parameters from kinetic treatment of data for the adsorption of MB onto the zinc oxide-doped activated carbon nanocomposite.

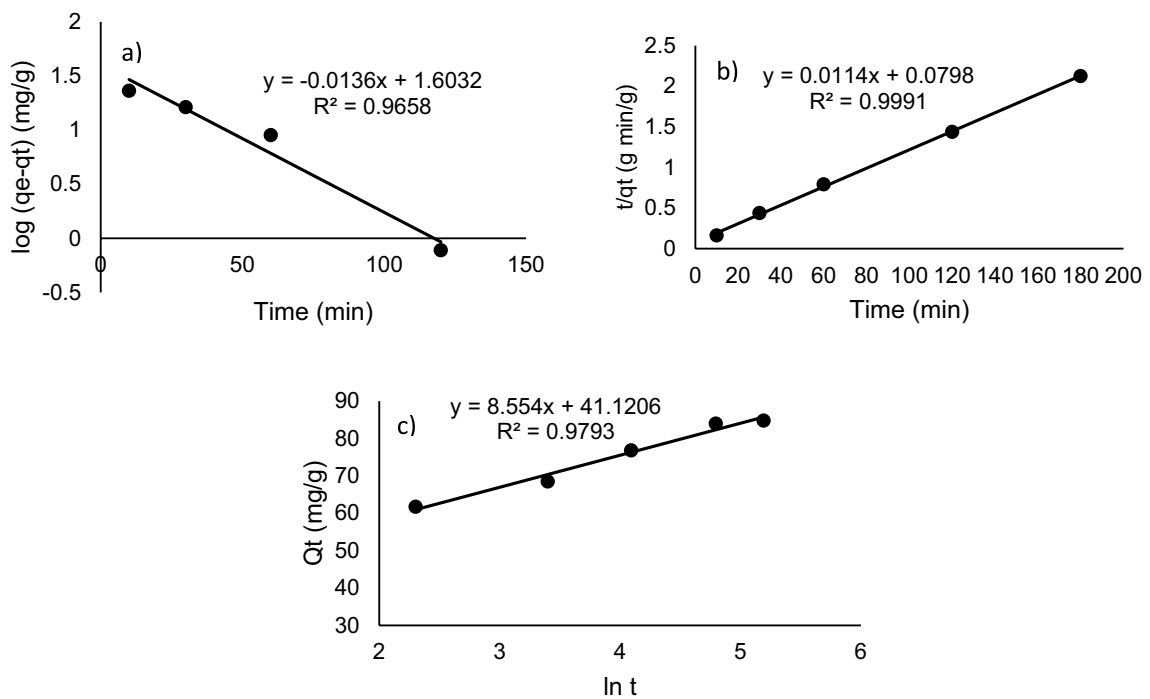


Fig. 9. Kinetic model plots for (a) Pseudo-first order (b) Pseudo-second order and (c) Elovich model.

systems⁴⁶. Information on the study of adsorption kinetics not only helps to deduce the value of the rate constants, but also tells the nature of adsorption—whether physisorption or chemisorption⁴⁷. As presented in Table 2, the pseudo-second order model (Fig. 9b) has a high R^2 of 0.9991 compared to the pseudo-first order (Fig. 9a) and Elovich models (Fig. 9c). This is an indication that the adsorption of MB onto the ZAC is better represented by the pseudo-second order model^{47,48}. The kinetic results also reveal that the adsorption process is more inclined towards the chemisorption nature of adsorption⁴⁸.

Regeneration study of ZAC

The regeneration study of ZAC highlights its potential for sustainable application in dye adsorption processes, with each regeneration method revealing distinct trends over five cycles as shown in Fig. 10. The thermal regeneration process exhibited the most consistent and effective results, with only a minor decline in adsorption capacity from 240 to 215 mg/g. This underscores the high thermal stability of ZAC, marking it a viable option where heat-based regeneration is feasible. Conversely, chemical regeneration using a mild acidic solution showed

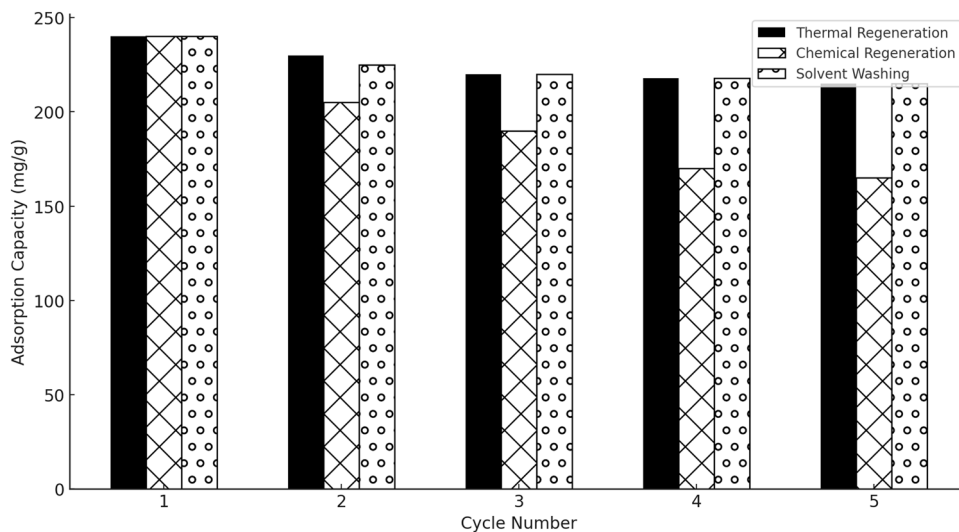


Fig. 10. Comparative analysis of ZAC regeneration methods over five cycles.

Adsorbent	Method of synthesis	Adsorbate	Maximum quantity/percentage adsorbed	References
Activated carbon developed from <i>Rumex abyssinicus</i> plant	Chemical and thermal activation methods	Methylene blue	99.9% removal efficiency	⁵⁰
Fig leaf activated carbon (FLAC)	Thermal carbonisation	Methylene blue	41.7 mg/g for MB removal	⁵¹
MgFe ₂ O ₄ nanoparticles	Commercial	Methylene blue	537.63 mg/g	⁵²
CN-Fe ₂ O ₃ NPs	Green synthesis using <i>Cola nitida</i> (CN) leaves extract,	Methylene blue and methyl orange	530.406 mg/g and 527.835 mg/g	⁵³
Raw groundnut shell biosorbent	Green synthesis	Methylen blue	29.3 mg/g for 50 mg/L MB concentration	⁵⁴
Zinc oxide doped activated carbon nanocomposites (ZAC)	Green synthesis	Phenothiazine model dye (MB)	248 mg/g (70.9%) for 140 mg/L MB concentration	Present study

Table 3. Comparison of different adsorbents with the present study.

a more pronounced decrease in capacity. Starting at 240 mg/g, it dropped significantly to 165 mg/g by the fifth cycle. This suggests that chemical treatment might be altering ZAC's surface chemistry or leading to pore blockage, indicating potential long-term drawbacks^{41,42,49}. Solvent washing with ethanol, while not as efficient as thermal regeneration, showed a relatively gentle and consistent impact on the adsorption capacity. It preserved most of ZAC's initial capacity, only reducing from 240 to 215 mg/g. This method could be suitable in scenarios where preserving the integrity of ZAC's structure is crucial. Overall, this study underscores the importance of selecting an appropriate regeneration technique based on the specific requirements of practical applications. Each method has its own set of advantages and limitations. Thermal regeneration stands out for its efficiency and consistency, making it suitable for applications where high-performance recovery is essential. Chemical regeneration, despite its initial effectiveness, may pose risks of structural deterioration in the long term. Solvent washing appears as a viable middle ground, offering a balance between efficacy and structural preservation. This subtle understanding of each method's impact is crucial for optimizing the use of ZAC in diverse environmental applications.

The Table 3 predominantly showcases adsorbents synthesized through green methods. For instance, the use of raw groundnut shell as a biosorbent for MB has shown a maximum uptake of 29.3 mg/g. This is particularly noteworthy in comparison with this study involving zinc oxide activated carbon for MB adsorption. Typically, zinc oxide activated carbon composites are valued for their enhanced adsorption properties due to the synergistic effect of zinc oxide's photocatalytic capability and the high surface area of activated carbon. Consequently, as observed in the Table 3, ZAC performed better than raw groundnut shells and other adsorbents though at different concentrations of MB which can be attributed to the presence of the zinc oxide nanoparticles. This highlights the potential of green synthesis methods in creating effective nanosorbents with lesser environmental impacts and better adsorption capacities.

Conclusions

Green synthesis is preferable to the traditional chemical synthesis of nanoparticles due to its lower costs, reduced pollution and enhanced safety for both human health and the environment. ZAC nanocomposite produced through a bioreduction process involving the application of *Nymphaea lotus* leaf extract as the reducing agent efficiently removes MB molecules from aqueous media. The crystalline, irregular shaped, and widely dispersed synthetic ZAC particles have an average size of 45 nm. The effectiveness of ZAC adsorption is determined by the initial MB concentration of the MB, the solution's pH, the ZAC dosage, and the contact time of ZAC and MB. The adsorption kinetics depends on the availability of adsorption sites and follows the pseudo-second order kinetic model, whereas, the adsorptive binding of MB on ZAC is best approximated by the Freundlich isotherm model and occurs through the chemisorption mechanism. Experimental results showed that the optimum quantity of MB adsorbed was 248 mg/g at MB concentration of 140 mg/L, 60 min contact time using 0.02 g/100 mL of ZAC. Thus, the synthesised ZAC could be beneficial in the textile or dye industries to the remediation of MB or other dye-laden contaminated wastewater.

Data availability

The datasets used and/or analysed during the current study available from the corresponding author on reasonable request.

Received: 11 June 2024; Accepted: 26 August 2024

Published online: 16 September 2024

References

1. Abdulla, N. K. *et al.* Silver based hybrid nanocomposite: A novel antibacterial material for water cleansing. *J. Clean. Prod.* **284**, 124746 (2021).
2. Abid, M. A., Abid, D. A., Aziz, W. J. & Rashid, T. M. Iron oxide nanoparticles synthesized using garlic and onion peel extracts rapidly degrade methylene blue dye. *Phys. B Condens. Matter* **622**, 413277 (2021).
3. Badawi, A. K. & Zaher, K. Hybrid treatment system for real textile wastewater remediation based on coagulation/flocculation, adsorption and filtration processes: Performance and economic evaluation. *J. Water Proc. Eng.* **40**, 101963 (2021).
4. Bayantong, A. R. B. *et al.* Adsorptive removal of dye in wastewater by metal ferrite-enabled graphene oxide nanocomposites. *Chemosphere* **274**, 129518 (2021).

5. Adesina, A. O., Elvis, O. A., Mohallem, N. D. S. & Olusegun, S. J. Adsorption of Methylene blue and Congo red from aqueous solution using synthesized alumina-zirconia composite. *Environ. Technol.* **42**, 1061–1070 (2021).
6. Ahmad, M. A., Eusoff, M. A., Oladoye, P. O., Adegoke, K. A. & Bello, O. S. Optimization and batch studies on adsorption of Methylene blue dye using pomegranate fruit peel-based adsorbent. *Chem. Data Coll.* **32**, 100676 (2021).
7. Chemingui, H. *et al.* Investigation of methylene blue adsorption from aqueous solution onto ZnO nanoparticles: Equilibrium and Box-Behnken optimisation design. *Int. J. Environ. Anal. Chem.* **103**, 2716–2741 (2021).
8. Çalimli, M. H. Magnetic nanocomposite cobalt-multiwalled carbon nanotube and adsorption kinetics of methylene blue using an ultrasonic batch. *Int. J. Environ. Sci. Technol.* **18**, 723–740 (2021).
9. Fito, J., Abrham, S. & Angassa, K. Adsorption of methylene blue from textile industrial wastewater onto activated carbon of *Parthenium hysterophorus*. *Int. J. Environ. Res.* **14**, 501–511 (2020).
10. Sen, T. K. Application of synthesized biomass bamboo charcoal-iron oxide “BC/Fe” nanocomposite adsorbents in the removal of cationic methylene blue dye contaminants from wastewater by adsorption. *Sustainability* **15**, 8841 (2023).
11. Dai, C., Zhang, M., Guo, X. & Ma, X. Mesoporous composite Ni-C-N/SA for selective adsorption of methylene blue from water. *Chem. Eng. J.* **407**, 127181 (2021).
12. Dinh, H. T., Tran, N. T. & Trinh, D. X. Investigation into the adsorption of methylene blue and methyl orange by UiO-66-NO₂ nanoparticles. *J. Anal. Methods Chem.* **2021**, 5512174 (2021).
13. El-Sayed, M. M. H. *et al.* Novel nanoporous membranes of bio-based cellulose acetate, poly(lactic acid) and biodegradable polyurethane in-situ impregnated with catalytic cobalt nanoparticles for the removal of methylene blue and congo red dyes from wastewater. *Carbohydr. Polym. Technol. Appl.* **2**, 100123 (2021).
14. Farghali, M. A., Abo-Aly, M. M. & Salaheldin, T. A. Modified mesoporous zeolite-A/reduced graphene oxide nanocomposite for dual removal of methylene blue and Pb²⁺ ions from wastewater. *Inorg. Chem. Commun.* **126**, 108487 (2021).
15. Nassar, M. Y., NourEldien, M. S., Ibrahim, I. M. & Aly, H. M. A facile hydrothermal synthesis of S-VO₂-cellulose nanocomposite for photocatalytic degradation of methylene blue dye. *Processes* **11**, 1322 (2023).
16. Aljohani, M. M., Masoud, E. M., Mohamed, N. M. & Nassar, M. Y. Cobalt aluminate/carbon nanocomposite via an auto-combustion method: An efficient photocatalyst for photocatalytic degradation of organic dyes from aqueous media. *Int. J. Environ. Anal. Chem.* **103**, 7979–7999 (2023).
17. Meselhy, G. M., Nassar, M. Y., Nassar, I. M. & Seda, S. H. lanthanum-doped TiO₂ nanostructures for efficient photocatalytic degradation of crystal violet dye. *Mater. Res. Innov.* <https://doi.org/10.1080/14328917.2024.2304927> (2024).
18. Sharma, K. *et al.* Methylene blue dye adsorption from wastewater using hydroxyapatite/gold nanocomposite: Kinetic and thermodynamics studies. *Nanomater.* **11**, 1403 (2021).
19. Nassar, M. Y., Moustafa, M. M. & Taha, M. M. Hydrothermal tuning of the morphology and particle size of hydrozincite nanoparticles using different counterions to produce nanosized ZnO as an efficient adsorbent for textile dye removal. *RSC Adv.* **6**, 42180–42195 (2016).
20. Shaibu, S. E., Inam, E. J. & Moses, E. A. Biogenic silver kaolinite nanocomposite for the sequestration of lead and cadmium in simulated produced water. *J. Mater. Environ. Sustain. Res.* **1**, 13–25 (2022).
21. Ituen, E. *et al.* Synthesis and characterization of walnut husk extract-silver nanocomposites for removal of heavy metals from petroleum wastewater and its consequences on pipework steel corrosion. *J. Mol. Liq.* **335**, 116132 (2021).
22. Nassar, M. Y. *et al.* Synthesis and characterization of lemon leaf extract-mediated silver nanoparticles: An environmentally friendly approach with enhanced antibacterial efficacy. *J. Mol. Struct.* **1315**, 138753 (2024).
23. Selvaraj, R. *et al.* Synthesis of magnetic biochar composite using *Vateria indica* fruits through in-situ one-pot hydro-carbonization for Fenton-like catalytic dye degradation. *Environ. Res.* **250**, 118414 (2024).
24. Samanth, A., Selvaraj, R., Murugesan, G., Varadavenkatesan, T. & Vinayagam, R. Efficient adsorptive removal of 2, 4-dichlorophenoxyacetic acid (2, 4-D) using biomass derived magnetic activated carbon nanocomposite in synthetic and simulated agricultural runoff water. *Chemosphere* **361**, 142513 (2024).
25. Selvaraj, R. *et al.* Machine learning and statistical physics modeling of tetracycline adsorption using activated carbon derived from *Cynometra ramiflora* fruit biomass. *Environ. Res.* **252**, 118816 (2024).
26. Enin, G. N., Shaibu, S. E., Ujah, G. A., Ibu, R. O. & Inangha, P. G. Phytochemical and nutritive composition of *Uvaria chamae* P. Beauv. leaves, stem bark, and root bark. *ChemSearch J.* **12**, 9–14 (2021).
27. Rege, M. G., Ayanwuyi, L. O., Zezi, A. U. & Odoma, S. Anti-nociceptive, anti-inflammatory and possible mechanism of anti-nociceptive action of methanol leaf extract of *Nymphaea lotus* Linn (Nymphaeaceae). *J. Tradit. Complement. Med.* **11**, 123–129 (2021).
28. Benzidia, B. *et al.* Chemical composition and antioxidant activity of tannins extract from green rind of *Aloe vera* (L.) Burm. *F. J. King Saud Univ. Sci.* **31**, 1175–1181 (2019).
29. Ajitha, B., Reddy, Y. A. K., Jeon, H. J. & Ahn, C. W. Synthesis of silver nanoparticles in an eco-friendly way using *Phyllanthus amarus* leaf extract: Antimicrobial and catalytic activity. *Adv. Powder Technol.* **29**, 86–93 (2018).
30. Adebayo, G. B. *et al.* Comparative study on the adsorption capacity and kinetics of xylene onto rice husk and cassava peel activated carbon. *Int. J. Curr. Res.* **11**, 8282–8288 (2019).
31. Garg, D. *et al.* Synthesis of silver nanoparticles utilizing various biological systems: Mechanisms and applications-a review. *Prog. Biomater.* **9**, 81–95 (2020).
32. Özsın, G., Kılıç, M., Apaydın-Varol, E. & Pütün, A. E. Chemically activated carbon production from agricultural waste of chickpea and its application for heavy metal adsorption: Equilibrium, kinetic, and thermodynamic studies. *Appl. Water Sci.* **9**, 1–14 (2019).
33. Majd, M. M., Kordzadeh-Kermani, V., Ghalandari, V., Askari, A. & Sillanpää, M. Adsorption isotherm models: A comprehensive and systematic review (2010–2020). *Sci. Total Environ.* **812**, 151334 (2022).
34. Sidhu, A. K., Verma, N. & Kaushal, P. Role of biogenic capping agents in the synthesis of metallic nanoparticles and evaluation of their therapeutic potential. *Front. Nanotechnol.* **3**, 801620 (2022).
35. Nadagouda, M. N. & Varma, R. S. Green synthesis of silver and palladium nanoparticles at room temperature using coffee and tea extract. *Green Chem.* **10**, 859–862 (2008).
36. Roseline, T. A., Murugan, M., Sudhakar, M. P. & Arunkumar, K. Nanopesticidal potential of silver nanocomposites synthesized from the aqueous extracts of red seaweeds. *Environ. Technol. Innov.* **13**, 82–93 (2019).
37. Elegami, A. A. *et al.* Two very unusual macrocyclic flavonoids from the water lily *Nymphaea lotus*. *Phytochemistry* **63**, 727–731 (2003).
38. Zubair, M., Aziz, H. A., Ihsanullah, I., Ahmad, M. A. & Al-Harthi, M. A. Engineered biochar supported layered double hydroxide-cellulose nanocrystals composite: Synthesis, characterization and azo dye removal performance. *Chemosphere* **307**, 136054 (2022).
39. Aziz, M. *et al.* Efficient removal of lead and chromium from aqueous media using selenium based nanocomposite supported by orange peel. *Front. Environ. Sci.* **10**, 947827 (2022).
40. Fakhari, S., Jamzad, M. & KabiriFard, H. Green synthesis of zinc oxide nanoparticles: A comparison. *Green Chem. Lett. Rev.* **12**, 19–24 (2019).
41. Singh, N., Singh, R., Shah, K. & Pramanik, B. K. Green synthesis of zinc oxide nanoparticles using lychee peel and its application in anti-bacterial properties and CR dye removal from wastewater. *Chemosphere* **327**, 138497 (2023).
42. Awe, A. A. *et al.* Preparation and characterisation of activated carbon from *Vitis vinifera* leaf litter and its adsorption performance for aqueous phenanthrene. *Appl. Biol. Chem.* **63**, 1–17 (2020).

43. Paredes-Quevedo, L. C., González-Caicedo, C., Torres-Luna, J. A. & Carriazo, J. G. Removal of a textile azo-dye (basic red 46) in water by efficient adsorption on a natural clay. *Water Air Soil Pollut.* **232**, 1–19 (2021).
44. Boudechiche, N. *et al.* Comparative study on removal of two basic dyes in aqueous medium by adsorption using activated carbon from *Ziziphus lotus* stones. *Microchem. J.* **146**, 1010–1018 (2019).
45. Usgodaarachchi, L., Thambiliyagodage, C., Wijesekera, R. & Bakker, M. G. Synthesis of mesoporous silica nanoparticles derived from rice husk and surface-controlled amine functionalization for efficient adsorption of methylene blue from aqueous solution. *Curr. Res. Green Sustain. Chem.* **4**, 100116 (2021).
46. Ho, Y. S. & McKay, G. Pseudo-second order model for sorption processes. *Process Biochem.* **34**, 451–465 (1999).
47. Raliya, R. & Tarafdar, J. C. Biosynthesis and characterization of zinc, magnesium and titanium nanoparticles: An eco-friendly approach. *Int. Nano Lett.* **4**, 93 (2014).
48. Minhas, L. A. *et al.* Green synthesis of zinc oxide nanoparticles using *Nostoc* sp. and their multiple biomedical properties. *Catalysts* **13**, 549 (2023).
49. Singh, V., Singh, J. & Mishra, V. Development of a cost-effective, recyclable and viable metal ion doped adsorbent for simultaneous adsorption and reduction of toxic Cr(VI) ions. *J. Environ. Chem. Eng.* **9**, 105124 (2021).
50. Fito, J. *et al.* Adsorption of methylene blue from textile industrial wastewater using activated carbon developed from *Rumex abyssinicus* plant. *Sci. Rep.* **13**, 5427. <https://doi.org/10.1038/s41598-023-32341-w> (2023).
51. Al-Asadi, S. T. *et al.* Adsorption of methylene blue dye from aqueous solution using low-cost adsorbent: Kinetic, isotherm adsorption, and thermodynamic studies. *Environ. Monit. Assess.* **195**, 676. <https://doi.org/10.1007/s10661-023-11334-245> (2023).
52. Al-Wasidi, A. S., Algethami, F. K., Saad, F. A. & Abdelrahma, E. A. Remarkable high adsorption of methylene blue dye from aqueous solutions using facilely synthesized MgFe₂O₄ nanoparticles. *J. Inorg. Organomet. Polym.* **33**, 2035–2045 (2023).
53. Mbachu, C. A. *et al.* Green synthesis of iron oxide nanoparticles by Taguchi design of experiment method for effective adsorption of methylene blue and methyl orange from textile wastewater. *Results Eng.* **19**, 101198 (2023).
54. Muzakir, M. M. & Joshua, J. Kinetics and thermodynamics of sorption of methylene blue dye onto raw groundnut shell biosorbent. *J. Environ. Bioremediat. Toxicol.* **6**, 1–7 (2023).

Acknowledgements

The authors gratefully acknowledge the financial support provided by the National Research Foundation (NRF) of South Africa (TTK170422228302). Additionally, this research was made possible through the generous support Nelson Mandela University.

Author contributions

Conceptualization: C.O.O., S.E.S., G.N.E., Z.R.T.; Methodology: S.E.S.; Formal analysis and investigation: S.E.S.; Writing—original draft preparation: S.E.S., T.J.A., D.P.F., U.A.O., O.K.F., N.E.E.; Writing -review and editing: S.E.S., O.S.A., O.Y.A., E.B.I., I.B.A., U.U.U., I.O.E., S.G.A.; Funding acquisition: C.O.O.; Resources: C.O.O., S.E.S., Z.R.T., S.M.N., M.J.K.

Competing interests

The authors declare no competing interests.

Additional information

Correspondence and requests for materials should be addressed to O.S.A.

Reprints and permissions information is available at www.nature.com/reprints.

Publisher's note Springer Nature remains neutral with regard to jurisdictional claims in published maps and institutional affiliations.

Open Access This article is licensed under a Creative Commons Attribution-NonCommercial-NoDerivatives 4.0 International License, which permits any non-commercial use, sharing, distribution and reproduction in any medium or format, as long as you give appropriate credit to the original author(s) and the source, provide a link to the Creative Commons licence, and indicate if you modified the licensed material. You do not have permission under this licence to share adapted material derived from this article or parts of it. The images or other third party material in this article are included in the article's Creative Commons licence, unless indicated otherwise in a credit line to the material. If material is not included in the article's Creative Commons licence and your intended use is not permitted by statutory regulation or exceeds the permitted use, you will need to obtain permission directly from the copyright holder. To view a copy of this licence, visit <http://creativecommons.org/licenses/by-nc-nd/4.0/>.

© The Author(s) 2024